Human Identification Using Palm-Vein Images

Yingbo Zhou and Ajay Kumar, *Senior Member, IEEE*

***Abstract*—This paper presents two new approaches to improve the performance of palm-vein-based identification systems presented in the literature. The proposed approach attempts to more effectively accommodate the potential deformations, rotational and translational changes by encoding the orientation preserving features and utilizing a novel region-based matching scheme. We systematically compare the previously proposed palm-vein identification approaches with our proposed ones on two different databases that are acquired with the contactless and touch-based imaging setup. We evaluate the performance improvement in both verification and recognition scenarios and analyze the influence of enrollment size on the performance. In this context, the proposed approaches are also compared for its superiority using single image enrollment on two different databases. The rigorous experimental results presented in this paper, on the databases of 100 and 250 subjects, consistently conforms the superiority of the proposed approach in both the verification and recognition scenario.**

***Index Terms*—Biometrics, hand biometrics, multispectral palmprint, palm-vein recognition, personal identification, vascular biometrics.**

I. Introduction

AUTOMATED human identification is one of the most critical and challenging tasks to meet growing demand for stringent security. The usage of physiological and/or behavioral characteristics of humans, i.e., biometrics, has been extensively employed in the identification of criminals and matured as an essential tool for law enforcement departments. The biometrics-based automated human identification is now highly popular in a wide range of civilian applications and has a become powerful alternative to traditional (password or token) identification systems. Human palms are easier to present for imaging and can reveal a variety of information. Therefore, palmprint research has invited a lot of attention for civilian and forensic usage [1]. However, like some of the popular biometrics (e.g., fingerprint [3], [4], iris [5], face [2], [6]), the palmprint biometric is also prone to sensor level spoof attacks. Remote imaging using a high-resolution camera can be employed to reveal important palmprint details for possible spoof attacks and impersonation. Therefore, *extrinsic* biometric features are expected to be more vulnerable for spoofing with moderate efforts. In summary, the advantages of easy accessibility of these *extrinsic* biometric traits also generate some concerns on privacy and security. On the other hand, *intrinsic* biometrics characteristics (e.g., DNA, vessel structures) require more challenging efforts to acquire without the knowledge of an individual and, therefore, more difficult to forge. However, in civilian applications it is also crucial for a biometrics trait to ensure high collectability while the user interacts with the biometrics device. In this context, palm-vein recognition has emerged as a promising alternative for personal identification. It has the advantage of the high agility but at the same time also ensures that the crucial identity information is unrevealed, therefore providing higher security and privacy for the user.

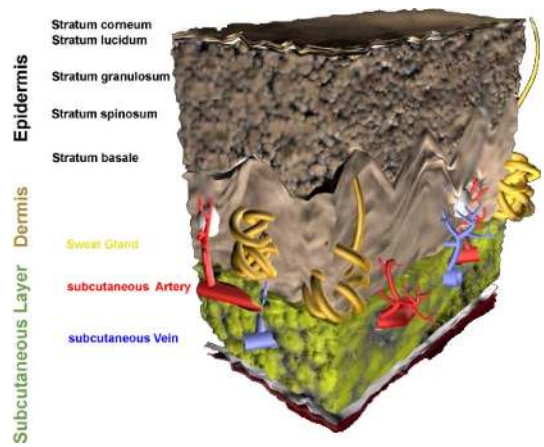

Fig. 1. Cross section anatomy of palmer skin [7].

The cross section of human skin which observes three key components of the skin, i.e., the outermost epidermis, dermis, and subcutaneous layer, is illustrated in Fig. 1. All three layers contain fat and blood with different proportions and it is the subcutaneous layer that contains subcutaneous veins and arteries. Different skin layers have different responses to the wavelength of the incident illumination [8]. The optical penetration depth [1] for near-infrared imaging at 850 nm is estimated to be 3.57 mm and such illumination has shown to offer higher contrast for the subcutaneous veins while imaging [26]. Therefore, the low-cost palm-vein imaging devices employing infrared illumination and a convention imaging sensor can acquire subcutaneous vein patterns from the presented palms for secured personal identification.

A. Related Work

The palm-vein imaging typically requires infrared illumination which is one component of multispectral illumination for the multispectral palmprint imaging. Therefore, the multispectral palmprint images inherently acquire palm-vein details. However, as compared to the bispectral approaches, such as in

Manuscript received October 30, 2010; revised May 09, 2011; accepted May 09, 2011. Date of publication June 02, 2011; date of current version November 18, 2011. This work was supported by the competitive research grant from The Hong Kong Polytechnic University (2010–2011) under Grant A-PK44 (PolyU 5181/10E). The associate editor coordinating the review of this manuscript and approving it for publication was Dr. Fabio Scotti.

Y. Zhou was with the Department of Computing, The Hong Kong Polytechnic University, Hung Hom, Kowloon, Hong Kong. He is now with the State University of New York at Buffalo, Buffalo, NY 14228 USA.

A. Kumar is with the Department of Computing, The Hong Kong Polytechnic University, Hung Hom, Kowloon, Hong Kong (e-mail: ajaykr@ieee.org).

Color versions of one or more of the figures in this paper are available online at http://ieeexplore.ieee.org.

Digital Object Identifier 10.1109/TIFS.2011.2158423

[1]Tissue thickness at which the light intensity reduces to 37% of its intensity on the surface [27].

[10], multispectral methods [11] introduce a significant amount of additional computations (which often adds to the cost of device) while achieving very little or marginal performance improvement. In the following, we briefly summarize the methods that have been proposed in the literature for human identification using palm-vein images. The approaches can be broadly categorized in two categories on the basis of the nature of extracted features.

1) **Holistic approaches using subspace learning**: Subspace learning has emerged as a powerful technique in which the palm-vein images are projected into subspaces built from training data. Various subspaces have been explored for the palm-vein identification: principle component analysis (PCA) and locality preserving projection (LPP) in [10], scale invariant feature transform (SIFT) in [17]. The subspace learning generates subspace coefficients (features) which are employed during the matching stage for the identification.
2) **Line/curve matching using vessel extraction**: The palm-vein images depict vascular structures and, therefore, the extraction of such curve- or line-like features have invited a lot of research focus. The (often) unclear palm-vein region of interest (ROI) images are extracted using spatial domain filtering. Several filters have been investigated for this purpose: Gabor filters [9], orthogonal Gaussian filters [11], cutoff Gaussian filters [13], matched filters [14], [15], and SUSAN edge detector [16]. The extracted line features are further encoded to form a template and employed during the identification.

The summary of prior work in the literature suggests the lack of any study to systematically compare the suitability of different feature representations for the palm-vein over different imaging setup protocols, such as contact free in [11] and [12] and constrained in [9], [10], [13], [14], [16], and [17]. In addition, the prior efforts have been more focused on the multispectral[2] palm images, rather than on single (near-infrared) spectrum palm-vein images. This has motivated us to further explore the palm-vein identification for real-world applications and ascertain the best possible performance from the near-infrared-based palm-vein identification.

B. Our Work

A review of prior work on palm-vein identification presented in the previous section outlines the need for the comparative performance on the most promising palm-vein feature extraction and matching approaches. In addition, the previous efforts have been more focused on constrained rather than contactless images. The contactless palm-vein identification is more hygienic, can offer higher user acceptability, and preserves the vascular patterns from distortion and, therefore, deserves further research efforts.

The key contributions from this paper can be summarized as follows. First, this paper investigates two new approaches which extract two different types of palm-vein features and achieves most promising performance. The Hessian-phase-based approach investigated in this paper extracts/preserves the vessel structures by analyzing the eigenvalues of second-order derivative of the normalized palm-vein images. This approach offers a computationally efficient and most compact (minimum template size) alternative for generating palm-vein templates than the *existing* methods. The neighborhood matching Radon transform approach *achieves the best performance* as compared to the prior palm-vein identification approaches presented in the literature. Second, we present a systematic and comparative analysis of the proposed approaches in both contactless and constrained palm-vein imaging environment and ascertain the robustness of our methods over these two setups. To the best of our knowledge, there has not been any study to comparatively evaluate the approaches for the palm-vein verification and, therefore, such needed comparison is presented in this paper. Finally, this paper rigorously evaluates the recognition performance and analysis of the influence of enrollment size on the achievable accuracy. It is well known that minimum numbers of training samples are desirable in a civilian biometrics system to ensure better user acceptability. Therefore, we rigorously evaluate the performance for the palm-vein identification with the variation in the size of enrollment or training samples and ascertain the performance. The palm-vein literature has been highly focused on the verification problem and there are little or negligible efforts to ascertain the performance for the recognition problem. Therefore, this paper has also presented recognition performance from various (also proposed ones) approaches on the two different databases (please refer to Section IV) to comparatively ascertain the performance from various approaches.

The rest of this paper is organized as follows: Section II presents the details on the preprocessing steps that normalize the palm-vein images acquired from the completely contactless imaging. Section III describes our proposed feature extraction and matching approach for the automated palm-vein identification. The experimental results are presented in Section IV and Section V provides discussion on the observations from our experimental results, including simulation results for the rank-1 palm-vein identification. Finally, the key conclusions from this paper are summarized in Section VI.

II. Preprocessing

The palm-vein images in contactless imaging present a lot of translational and rotational variations. Therefore, more stringent preprocessing steps are required to extract a stable and aligned ROI. The preprocessing steps essentially recover a fixed-size ROI from the acquired images which have been normalized to minimize the rotational, translational, and scale changes. This is followed by the nonlinear enhancement so that the vein patterns from ROI images can be observed more clearly.

A. Image Segmentation and Normalization

The key objective while segmenting the ROI is to automatically normalize the region in such a way that the image variations, caused by the interaction of the user with the imaging device, can be minimized. In order to make the identification process more effective and efficient, it is necessary to construct a coordinate system that is invariant/robust (or nearly) to such variations. It is judicious to associate the coordinate system

[2]Using multiple sets of illuminators, where each set peaks the illumination at a specific wavelength at a time.

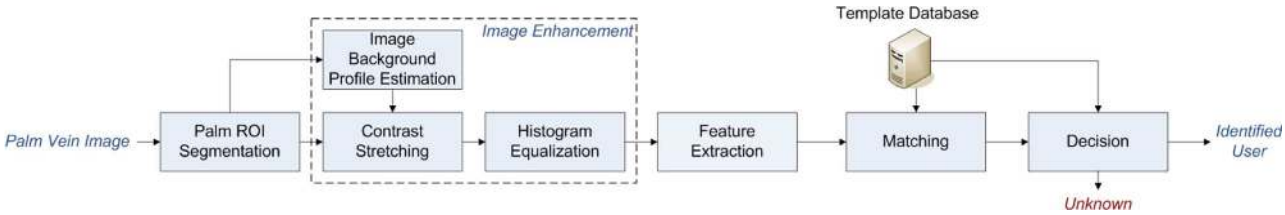

Fig. 2. Block diagram for personal identification using palm-vein images.

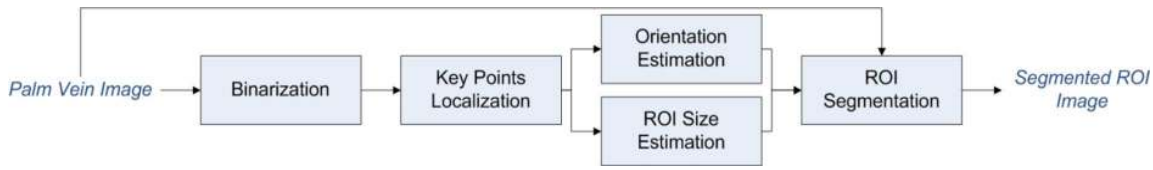

Fig. 3. Key steps in segmenting ROI images from contactless palm-vein images.

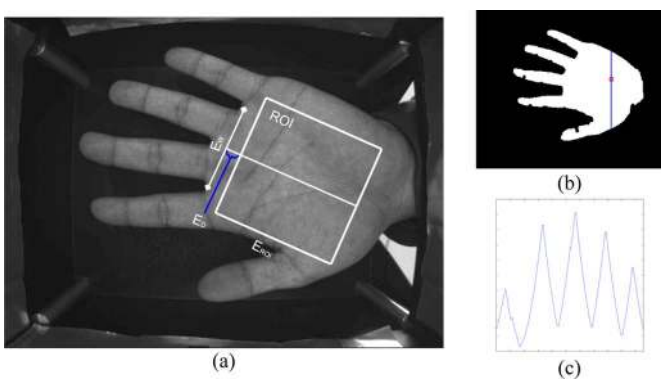

Fig. 4. Illustration of segmentation of palm-vein ROI from an (a) acquired sample image with the illustration of key points, (b) the binarized image of (a), and (c) the distance from the center of the palm [shown as a red dot in (b)] to the palm boundary [on the left side of the blue line in (b)].

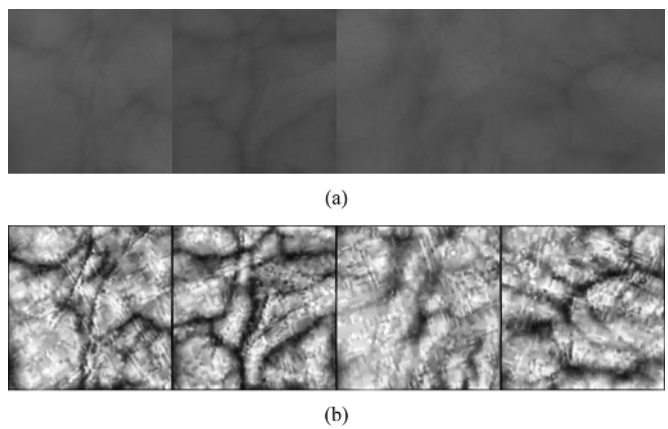

Fig. 5. Illustration of image enhancement: (a) original ROI images, (b) correspondingly enhanced ROI images of (a).

with the palm itself since we are seeking the invariance corresponding to it. Therefore, two webs are utilized as the reference points/line to build up the coordinate system, i.e., the web between the index finger and middle finger together with the web between the ring finger and little finger [Fig. 4(a)]. These web points are easily identified in touch-based imaging (using pegs) but should be automatically generated for contactless imaging.

The acquired palm images are first binarized [see Fig. 4(b)], so that we are able to separate the palm region from the background region. This is followed by the estimation of the distance from center position of the binarized palm to the boundary of palm [see Fig. 4(c)]. We locate the two webs by finding the corresponding local minima from the calculated distance. The potential scale changes in the contactless environment can be quite large, and in order to account for this variation, it is wise to adaptively select the location and size of the ROI according to certain image-specific measures from the palm. In our approach, we select these two parameters based on the distance between the two webs (E_W) and this process can be illustrated as follows:

$$\begin{cases} E_D = \eta E_W \\ E_{\mathrm{ROI}} = \xi E_W \end{cases} \tag{1}$$

where E_{ROI} denotes the size of the ROI, E_D denotes the distance between the ROI and the reference line, as shown in Fig. 4, and E_W represents the distance between the two webs. The η and ξ are the factors that respectively control the location and size of the ROI, which are determined experimentally from the training data. The approach employed in [11] may be similar to that in this work. However, our method is more computationally efficient since no additional sampling/computations are required. After segmentation, the ROI images are scaled to generate a fixed size region and the whole process is illustrated in Fig. 3.

B. Image Enhancement

The palm-vein images employed in our work were acquired under near-infrared illumination (NIR); the images generally appear darker with low contrast. Therefore, image enhancement to more clearly illustrate the vein and texture patterns is required. We first estimate the background intensity profiles by dividing the image into slightly overlapping 32×32 blocks (three pixels overlapping between two blocks to address the *blocky effect*), and the average gray-level pixels in each block are computed. Subsequently, the estimated background intensity profile is resized to the same size as the original image using bicubic interpolation and the resulting image is subtracted from the original ROI image. Finally, histogram equalization is employed to obtain the normalized and enhanced palm-vein image. As can be observed from Fig. 5, the enhancement has been quite successful in improving the details and contrast of the ROI images.

III. Feature Extraction and Matching

The normalized and enhanced palm-vein images depict curved vascular network/patterns, and these vessels can be

approximated by small line segments which are rather curved. Therefore, in this paper, we propose to use two new approaches to extract such line-like palm-vein features. In addition, a neighborhood matching scheme that can effectively account for more frequent rotational, translational variations, and also to some image deformations in the acquired image. This approach is detailed in Sections IV–VI.

A. Neighborhood Matching Radon Transform

The Radon transform [19] is an effective tool to identify continuous line structures in the images. The two-dimensional (2-D) Radon transform of a given function h is defined as follows:

$$\text{Radon}(k,b)[h(x,y)] = \int_{-\infty}^{+\infty}\int_{-\infty}^{+\infty} h(x,y)\delta[y-(kx+b)]dxdy \quad (2)$$

where k is the slope of the line and b is the intercept. Equation (2) illustrates the process of integration, for all the values from the domain of x and y, in a given image to locate the lines. Thus, if the length of the line is significantly shorter than the image dimension, then the process in (2) may not be able to locate that line which is really the case in detecting the palm-veins as line segments. In addition, the vessels may suddenly change their direction to an almost perpendicular orientation, and therefore breaking the long curve into several short line segments. To overcome this problem, it is intuitive to restrict the transformation in the local area and select the size of the local region to be small enough so that the target shortest line segments in the images can be detected. The localized Radon transform [18], [20], [21] utilizes this idea, and it further simplifies the transformation by fixing the intercept term and restricting the integration in a confined width (linewidth). Mathematically, it can be represented as in the following equation:

$$\text{LRT}_I(k) = \sum_{(x,y)\in l_k} I[x,y] \quad (3)$$

where I represents the normalized 2-D palm-vein image. We define $\mathfrak{U}_a = \{0,1,\ldots,a-1\}$, where a is a positive integer that indicates the minimum length of the line segment to extract/detect, and the center of $\mathfrak{U}_a^2$ is at (X_0,Y_0). Let l_k represent the set of points on $\mathfrak{U}_a^2$ such that

$$l_k = \{(x,y)|y = kx + c, x \in R_q\} \quad (4)$$

where k denotes the slope of the line l_k, $c = Y_0 - kX_0$ and l_k is the line passing through the center (x_0,y_0) of lattice $\mathfrak{U}_a^2$. Note that the center of $\mathfrak{U}_a^2$ is not necessarily a single point but it should have the same parity as a so that the line can be properly placed in the lattice. For example, in case of $a = 10$, (X_0,Y_0) can be four points (2×2), but cannot be one or nine points, and the size of X_0 (or Y_0) represents the width of the line l_k. Finally, the line in the lattice $\mathfrak{U}_a^2$ is encoded in the following manner:

$$D_o(x,y) = \arg\min_o(\text{LRT}_I(k)), o = 1,2,\ldots,O \quad (5)$$

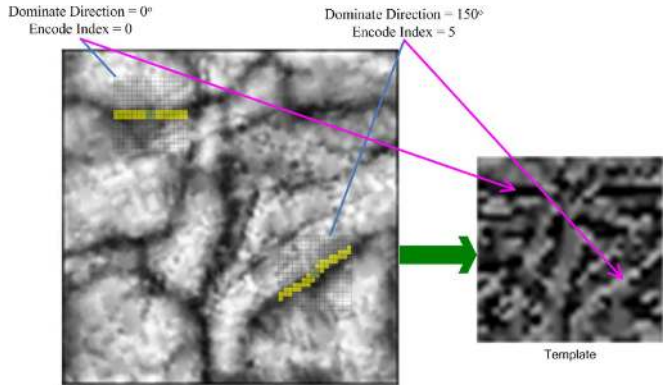

Fig. 6. Illustration of NMRT feature extraction.

where the $D_o(x,y)$ represents the estimated direction of pixel $I(x,y)$, and O denotes the number of line directions/slopes. This operation is repeated as the center of lattice $\mathfrak{U}_a^2$ moves over all the pixels in the image. At each position, the dominant orientation D_o is recorded to form the feature vector of the palm-vein image. Since the veins appear darker in the palm-vein images, the line direction that results in the minimum summation (integration) value is encoded as the dominant direction. It should be pointed out that this encoding scheme also accounts for the potential rotational changes to some extent, since it quantizes the directions of lines to only an O number of orientations (O is fixed to six in our experiments), and thus as long as the variation in orientation is not so severe (e.g., not more than $\pi/6$ in case of six directions), the resulting code will not be altered. Hence, the degree of robustness against rotational variations also depends on the number of orientations: a value that is too small will only be sensitive to larger variations, and as a result, the encoded template is not distinguishable. On the contrary, a value that is too big will lead to noisy templates that make the genuine match worse.

The resulting template size is inversely proportional to the linewidth, since each of the possible orientations of line segment is just encoded into one code, for a given/certain linewidth. This procedure is diagrammatically illustrated in Fig. 6 for a linewidth of two pixels, six orientation, and a lattice size 16×16.

The generation of matching scores between two encoded palm-vein templates can be quite straightforward using the following equation:

$$M(F_r,F_t) = \min_{\forall h\in[-m,m],\forall v\in[-n,n]}\left\{\frac{\text{hamdist}\left(F_r,F_t^{h,v}\right)}{\left\|F_r \cap F_t^{h,v}\right\|}\right\} \quad (6)$$

where F_r represents the registered palm-vein template, $F_t^{h,v}$ denotes the unknown test template translated by h and v pixels in horizontal and vertical directions, *hamdist* generates the hamming distance between two templates, i.e., summation of the number of positions that are different, m and n control the amount of translation in horizontal and vertical directions, respectively, and $\|\ \|$ is the cardinality operator. However, the matching score generated from (6) does not exploit local

information, which can be more stable and robust to imaging variations of image deformations. Therefore, we develop a new approach to robustly and reliably generate the matching scores using the local neighborhood information, which is shown to significantly improve the performance and described in the following.

Let R and P represent the palm-vein templates generated during the registration and validation/probe stages, respectively, $r_i^{w,h}$ and $p_i^{w,h}$ denote the connected subregion separated from the template with width w and height h, N represents for the total number of partitions, and then the region partitioning can be described by equation (7), shown at the bottom of the page. After partitioning the templates into disjointed subregions, we can use (8) to match the corresponding partitions

$$M(R,P) = M(\hat{R},\hat{P}) = \sum_{\forall Z \in N} \left\{ \min_{\forall h \in [-m,m], \forall v \in [-n,n]} \left\{ \frac{\text{hamdist}\left(r_Z, p_Z^{h,v}\right)}{\left\| r_Z \cap p_Z^{h,v} \right\|} \right\} \right\}. \tag{8}$$

By using (8), the matching takes the possible local variations into account by matching the subregions correspondingly with a small amount of shifting. Therefore, this approach is expected to be more robust against potential changes, that may occur more frequently with contactless imaging.

B. Hessian-Phase-Based Feature Extraction

The local palm-vein image characteristics can be observed using Taylor series expansion in the neighborhood of a point. The local characteristic of an image I considering its Taylor expansion in the neighborhood of a point p is shown as follows [22]:

$$I(p+\Delta p, s) \approx I(p,s) + J(p)\Delta p + \frac{1}{2}\Delta p^T H(p) \Delta p. \tag{9}$$

The above equation estimates the structure of the image up to the second order in scale s, where J and H denote for the Jacobian and Hessian matrix, respectively. The differentiation is defined as a convolution with the derivatives of the Gaussian functions

$$\frac{\partial}{\partial p} I(p,s) = sI(p) \star \frac{\partial}{\partial p} \mathcal{G}(p,s) \tag{10}$$

$$\mathcal{G}(p,s) = \frac{1}{\sqrt[N]{2\pi s^2}} e^{-\|p\|^2/2s^2} \tag{11}$$

where $\star$ is the convolution operator and $\mathcal{G}$ is the N-dimensional Gaussian function at scale s. Recall that the eigenvector of a matrix corresponds to the basis/principal directions of the matrix, and thus the magnitude of the corresponding eigenvalues of the Hessian matrix (second-order derivative) will reflect the curvature of the principal orientation in the local image. Let λ_m denote the eigenvalue with the mth smallest magnitude, for an ideal vessel-like structure in a 2-D image the eigenvalues should have the form as shown follows:

$$|\lambda_1| \approx 0 \tag{12}$$

$$|\lambda_2| \gg |\lambda_1|. \tag{13}$$

Two local characteristics of image can be measured by analyzing the above two equations. First, the norm of the eigenvalues will be small at the location where no structure information is shown since the contrast difference is low, and it will become larger when the region occupies higher contrast since at least one of the eigenvalues will be large. Second, the ratio between $|\lambda_1|$ and $|\lambda_2|$ will be large when the blob-like structure appears in the local area, and will be very close to zero when the structure shown is line-like. Mathematically, the two measures is represented as follows:

$$L_s = \sqrt{\sum_{i \le N} \lambda_i^2} \tag{14}$$

$$L_l = \frac{|\lambda_1|}{|\lambda_2|} \tag{15}$$

where L_s and L_l are the measures of the local structure and local line characteristics with N denoting the dimension of the image. Therefore, the local "vesselness" of position p in scale s is assigned using the following equations [22]:

$$V_p(s) = \begin{cases} 0, & \text{if } \lambda_2 < 0 \\ \exp\left(-\frac{L_l^2}{2a^2}\right)\left(1 - \exp\left(-\frac{L_S^2}{2b^2}\right)\right) \end{cases} \tag{16}$$

$$I_E(p) = \max_{\forall\ S \in S} V_p(s,p) \tag{17}$$

where a is fixed to 0.5 and b equals to half of the maximum Hessian norm, I_E represents for the enhanced image, and S is the set which contains all the defined scales. The enhanced image is then binarized to form the template (Hessian phase), the global thresholding does not give good performance in our experiment, since the enhanced vessel image occupies a relatively broad intensity range. Therefore, a localized binarization scheme [23] was investigated. Essentially this scheme creates two local windows, i.e., inner and outer window, and the local threshold value is selected based on the follows [23]:

$$T_{\text{bin}} = (1-\omega_1)\mu + h_1\left(\frac{\sigma_{\text{inner}}}{\sigma_{\text{outer}}}\right)^{\tau+1}(\mu - M) + \omega_2 M \tag{18}$$

$$\omega_2 = h_2\left(\frac{\sigma_{\text{inner}}}{\sigma_{\text{outer}}}\right)^{\tau} \tag{19}$$

$$\begin{cases} \hat{R} = \left\{ r_i^{w,h} | r_i^{w,h} \in R, r_i^{w,h} \cap r_j^{w,h} = \emptyset, i \neq j \text{ and } i,j = 1 \cdots N \right\} \\ \hat{P} = \left\{ p_i^{w,h} | p_i^{w,h} \in P, p_i^{w,h} \cap p_j^{w,h} = \emptyset, i \neq j \text{ and } i,j = 1 \cdots N \right\} \end{cases} \tag{7}$$

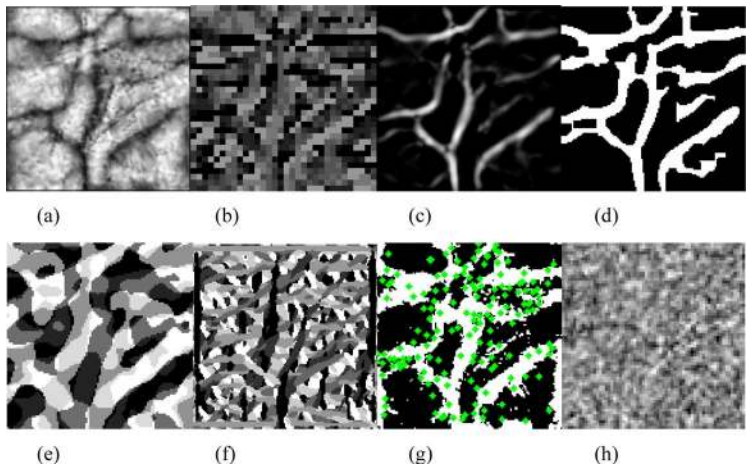

Fig. 7. Samples of image representation of extracted features, (a) the enhanced ROI image, (b) features extracted from (a) using LRT, (c) multiscale vessel enhancement of (a), (d) phase extracted from (c), (e) ordinal representation [11] of (a), (f) competitive code [9] representation of (a), (g) key points (in green) extracted by SIFT [17], and (h) Laplacian palm [10] representation of (a).

where μ, σ_{inner}, and M are the mean, standard deviation, and the minimum intensity value of the inner window, σ_{outer} represents for the standard deviation of the outer window, ω_1, h_1, h_2, and τ are constants and fixed to values 0.1, 0.25, 0.04, and 3, respectively, in this experiment. By using this binarization scheme, the threshold in the local area will have greater values where the vein structures appear, since the ratio of the standard deviation in the second and third term will be larger when the inner window covers the vein structure. In addition, in the area where no vein appears, the threshold is expected to be higher than the mean value so as to depress the possibility of noise enhancement from the true background regions. Fig. 7(d) illustrates the sample results from this approach. It can be noticed that the true vein structures are quite well preserved in the resulting binarized image. Equation (6) is then employed for computing the matching score between the binarized templates.

IV. Experiment and Results

In order to ascertain the effectiveness and robustness of the proposed approach for the palm-vein identification, we performed rigorous experiments on both contactless and contact-based databases. The extraction of palm-vein features using Gabor filters [9], Ordinal Code [11], and Laplacian palm [10] have been suggested in the literature with promising results. Scale invariant feature transform (SIFT) [12] has also been investigated in [17] and shown to offer high performance. Therefore, we systematically evaluated and compared all these methods together with our proposed ones, so that we can get more insights into the problem of palm-vein identification.

A. Database

In this work, we first the employed CASIA Multi-Spectral Palmprint Image Database V1.0 (CASIA database) [24] which has been acquired from the contactless palm imaging of 100 subjects. All the images have been acquired in two data acquisition sessions with a minimum interval of one month, and at each time three samples were acquired from each user. The second database employed in this work is the PolyU Multispectral Palmprint Database (PolyU database) [9], and all the images were acquired with a constrained device with finger-pegs, and is composed of images from 250 individuals with 12 images from each individual. These images were captured in two sessions (six images in each session) with an average interval of nine days. We employed these two databases, which are rather from an independent imaging setup, in our study so as to comparatively evaluate the performance from various methods and ascertain the robustness of our methods on different imaging setups. Since the focus of our work is on palm-vein identification, and the palm-vein images are largely observed in NIR, only the images that were acquired under 850-nm wavelength illumination from the CASIA database and near-infrared images from the PolyU database were used in the following experiments.

B. Identification Experiments

In order to reliably ascertain the performance of our proposed approach, we rigorously evaluated and compared the identification performance on two different databases. The samples from the first session were used as the gallery (i.e., the first three images from the CASIA database and first six images from the PolyU database), and the rest of the images served as the probe. The capability to achieve higher performance with a smaller number of training samples or registration samples is highly desirable in any biometrics system. In this context, the average performance evaluation with just one (minimum) training sample can be highly representative for the comparative performance evaluation. Therefore, in this study, we also present analysis of various palm-vein identification approaches when the numbers of training samples are varied.

We performed four experiments on each of the two databases; first the recognition performance from the individual (left and right hands) palm-vein image samples was investigated; second, we ascertained the performance by combining the left- and right-hand palm-vein samples while considering them as belonging to different classes; third, several image samples, i.e., images from the last ten subjects in the CASIA dataset and the last 50 subjects in the PolyU dataset, were removed from the gallery and their corresponding query samples were used as unknown subjects, i.e., subjects not registered in the gallery, and the experiments were repeated in a similar manner

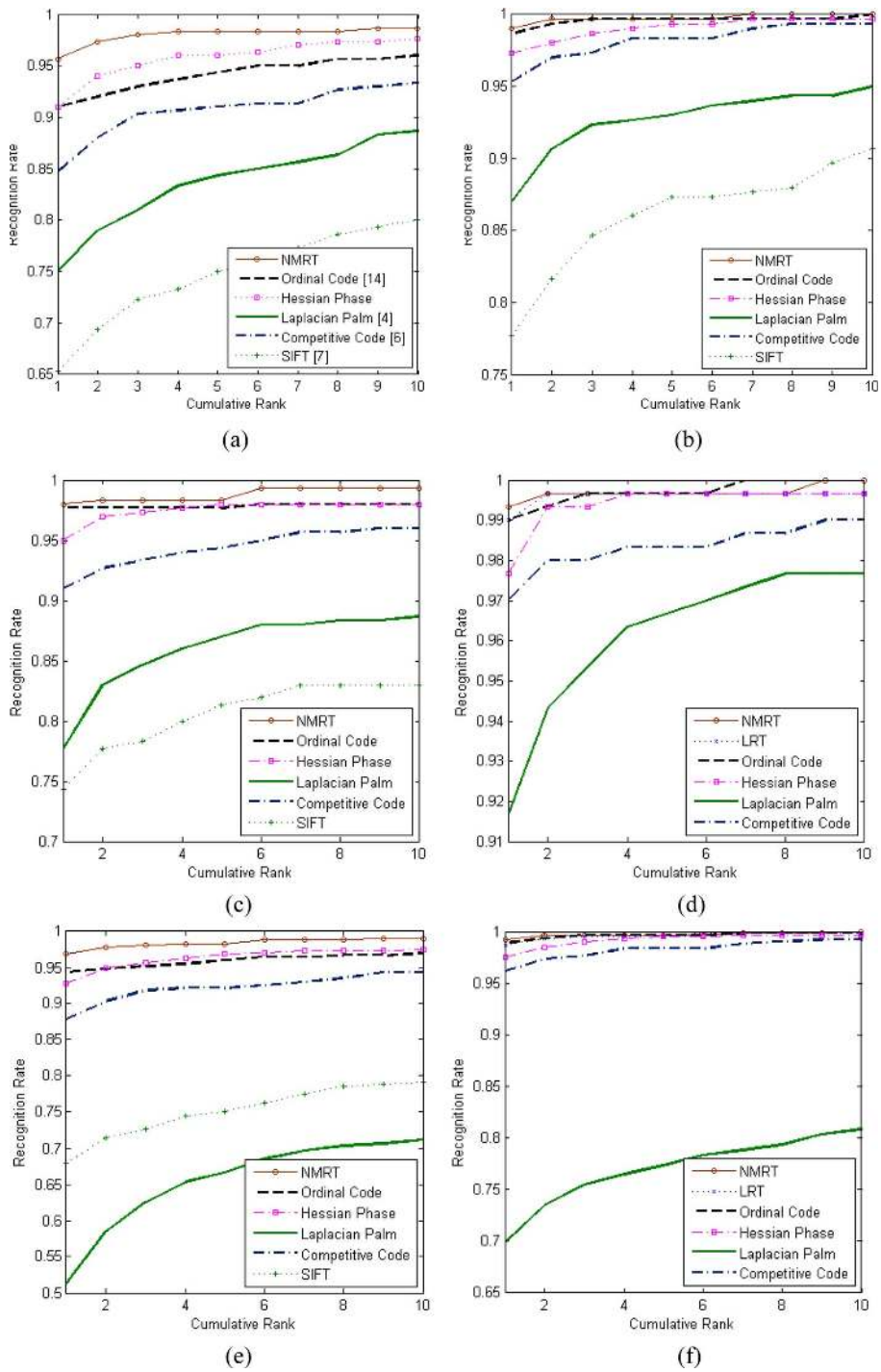

Fig. 8. Cumulative match characteristics of palm-vein images from the CASIA database with a different number of gallery samples for each subject: (a) and (b) show the performance from left palm using 1- and 3-gallery samples respectively; (c) and (d) show the performance from right palm using 1- and 3-training samples; and (e) and (f) show the performance from right and left palm using 1- and 3-gallery samples.

as the previous two cases. The key purpose of the third and fourth experiments is to ascertain the potential influence of unregistered users (outliers) to the performance of the system and to test the robustness of the individual method in such circumstances. The average rank-1 identification rates from the CASIA database are illustrated in Tables I–VI, and the cumulative match characteristics (CMCs) are shown in Fig. 8.

It can be observed from the presented results that our neighborhood matching Radon transform (NMRT) approach consistently outperforms other promising methods in all four experiments, especially in the case of a smaller number of gallery images for each class, which is contributed by the localized matching. Unlike other matching methods, the neighborhood matching scheme searches for the best match by translating/shifting in the local area between the corresponding region, which makes more effective use of the local information and, therefore, can accommodate higher deformation and image variations. In addition, it virtually increases the training samples by partitioning the template into separate regions (considering each region as training samples) and thus this *scheme*

TABLE I
RANK ONE IDENTIFICATION RATE FROM *ALL* LEFT PALMS IN THE CASIA DATABASE USING DIFFERENT APPROACHES WITH VARYING NUMBERS OF GALLERY IMAGES PER CLASS

Number of Gallery Samples per Class	NMRT	Hessian Phase	Ordinal Code	Laplacian Palm	Comp Code	SIFT
1	95.67%	91.00%	91.00%	75.00%	84.67%	65.33%
2	99.00%	96.00%	96.33%	83.33%	93.00%	73.00%
3	99.00%	97.33%	98.67%	87.00%	95.33%	77.67%

TABLE II
RANK ONE IDENTIFICATION RATE FROM *ALL* RIGHT PALMS IN THE CASIA DATABASE USING DIFFERENT APPROACHES WITH VARYING NUMBERS OF GALLERY IMAGES PER CLASS

Number of Gallery Samples per Class	NMRT	Hessian Phase	Ordinal Code	Laplacian Palm	Comp Code	SIFT
1	98.00%	95.00%	97.67%	77.67%	91.00%	74.33%
2	99.67%	96.67%	98.00%	86.33%	94.67%	82.00%
3	99.33%	97.67%	99.00%	91.67%	97.00%	86.00%

TABLE III
RANK ONE IDENTIFICATION RATE FROM *ALL* LEFT AND RIGHT PALMS IN THE CASIA DATABASE USING DIFFERENT APPROACHES WITH VARYING NUMBERS OF GALLERY IMAGES PER CLASS

Number of Gallery Samples per Class	NMRT	Hessian Phase	Ordinal Code	Laplacian Palm	Comp Code	SIFT
1	96.83%	92.83%	94.33%	51.33%	87.83%	68.00%
2	99.33%	96.33%	97.17%	59.00%	93.67%	75.67%
3	99.17%	97.50%	98.83%	69.83%	96.17%	80.83%

TABLE IV
COMPARATIVE RANK ONE IDENTIFICATION RATE FROM FIRST 90 LEFT PALMS IN THE CASIA DATABASE WITH 10 *UNKNOWN* SUBJECTS WITH VARYING NUMBERS OF GALLERY IMAGES PER CLASS

Number of Gallery Samples per Class	NMRT	Hessian Phase	Ordinal Code	Laplacian Palm	Comp Code	SIFT
1	95.56%	91.11%	91.11%	72.96%	84.07%	65.56%
2	98.89%	96.67%	95.56%	82.59%	93.33%	72.59%
3	99.26%	98.15%	97.78%	86.30%	95.56%	78.15%

TABLE V
COMPARATIVE RANK ONE IDENTIFICATION RATE FROM FIRST 90 RIGHT PALMS IN THE CASIA DATABASE WITH 10 *UNKNOWN* SUBJECTS WITH VARYING NUMBERS OF GALLERY IMAGES PER CLASS

Number of Gallery Samples per Class	NMRT	Hessian Phase	Ordinal Code	Laplacian Palm	Comp Code	SIFT
1	97.41%	94.81%	97.41%	77.04%	90.74%	73.70%
2	99.26%	96.30%	97.41%	86.30%	94.07%	81.85%
3	99.26%	97.04%	98.15%	92.22%	96.67%	86.30%

performs very well even under the minimum number of training cases (i.e., only one gallery sample for each class). As expected, the identification performance improves as the training samples increase, especially when the number of training samples was increased from one to two, all the methods have a significant improvement (about 10% increment in recognition rate). Therefore, for the dataset that is likely to have higher intraclass variations (e.g., contactless and unconstrained acquisition at a distance) as in the CASIA database, it is judicious to use more than one training sample for each class, since it is quite likely that the user may interact with the device differently at each time which will introduce intraclass variations. Therefore, the additional training samples in such contactless acquisition are more likely to contribute complementary information of the same class. The Laplacian palm method does not perform well in such cases, and a possible reason for its limited performance may lie in the fact that it utilizes only global features and does not account for the rotational and translational variations, which are quite common in this database.

The rank one identification rate from the experiments using the PolyU database is shown in Tables VII–XII. Unlike the CASIA experimental results, the performance improvement from the PolyU database may not be significant with the number of training samples increasing (except the case of Laplacianpalm), especially when the number of training samples is higher than three, and the plausible explanation for this could be due to the following reasons. First, as the finger-pegs were employed by the imaging device in the PolyU database, the image variations[3] from the same subject are observed to be much smaller than those from the CASIA database. In other words, the additional training sample does not bring much complementary/useful information and thus the resulting performance improvement is much smaller. On the contrary, the misplaced/improper samples can indeed deteriorate the performance (skew the matching scores generated from the matcher). Additionally, it should be pointed out that the performance from the PolyU database is already relatively high with smaller training cases, so the room for the noticeable improvement is much less as compared to the previous case. However, there is consistent performance gain from the Laplacian method; this may corresponds to the nature of locality preserving projection

[3]The absolute mean rotational variation estimated by our normalization approach from the left-hand palm-vein samples in the CASIA database is 21.0° but 3.1° in the PolyU database.

TABLE VI
COMPARATIVE RANK ONE IDENTIFICATION RATE FROM FIRST 90 LEFT AND FIRST 90 RIGHT PALMS IN THE CASIA DATABASE WITH 20 *UNKNOWN* SUBJECTS WITH VARYING NUMBERS OF GALLERY IMAGES

Number of Gallery Samples per Class	NMRT	Hessian Phase	Ordinal Code	Laplacian Palm	Comp Code	SIFT
1	96.11%	92.41%	93.52%	51.48%	87.04%	67.41%
2	98.89%	95.93%	96.67%	58.70%	93.15%	75.93%
3	99.07%	97.41%	98.15%	69.81%	95.74%	80.37%

TABLE VII
RANK ONE IDENTIFICATION RATE FROM *ALL* LEFT PALMS OF THE POLYU DATABASE USING DIFFERENT APPROACHES WITH VARYING NUMBERS OF GALLERY IMAGES PER CLASS

Number of Gallery Samples per Class	NMRT	Hessian Phase	Ordinal Code	Laplacian Palm	Comp Code	SIFT
1	99.40%	97.07%	98.67%	65.87%	92.40%	81.60%
2	99.60%	99.00%	99.20%	76.60%	95.47%	89.73%
3	100.00%	99.53%	99.93%	83.80%	97.87%	92.73%
4	100.00%	99.53%	99.93%	87.07%	98.00%	94.00%
5	100.00%	99.67%	99.93%	89.33%	98.53%	94.53%
6	100.00%	99.73%	99.93%	90.53%	99.07%	95.53%

TABLE VIII
RANK ONE IDENTIFICATION RATE FROM ALL *RIGHT* PALMS OF THE POLYU DATABASE USING DIFFERENT APPROACHES WITH VARYING NUMBERS OF GALLERY IMAGES PER CLASS

Number of Gallery Samples per Class	NMRT	Hessian Phase	Ordinal Code	Laplacian Palm	Comp Code	SIFT
1	99.93%	98.87%	100.00%	77.67%	92.80%	85.33%
2	100.00%	99.40%	100.00%	85.13%	96.67%	91.60%
3	100.00%	99.40%	100.00%	87.40%	97.93%	93.33%
4	100.00%	99.60%	100.00%	88.80%	98.80%	94.60%
5	100.00%	99.60%	100.00%	89.33%	98.80%	95.67%
6	100.00%	99.60%	100.00%	89.20%	98.87%	96.20%

TABLE IX
RANK ONE IDENTIFICATION RATE FROM *ALL* LEFT AND RIGHT PALMS OF THE POLYU DATABASE USING DIFFERENT APPROACHES WITH VARYING NUMBERS OF GALLERY IMAGES PER CLASS

Number of Gallery Samples per Class	NMRT	Hessian Phase	Ordinal Code	Laplacian Palm	Comp Code	SIFT
1	99.67%	97.90%	99.33%	63.13%	92.57%	83.13%
2	99.80%	99.23%	99.60%	72.17%	76.07%	90.17%
3	100.00%	99.47%	99.93%	76.67%	97.90%	92.57%
4	100.00%	99.57%	99.97%	79.60%	98.40%	94.13%
5	100.00%	99.63%	99.97%	81.13%	98.67%	94.93%
6	100.00%	99.63%	99.93%	82.73%	98.97%	95.50%

TABLE X
RANK ONE IDENTIFICATION RATE FROM FIRST 200 LEFT PALMS OF THE POLYU DATABASE WITH 50 *UNKNOWN* SUBJECTS WITH VARIATION IN NUMBERS OF GALLERY IMAGES PER CLASS

Number of Gallery Samples per Class	NMRT	Hessian Phase	Ordinal Code	Laplacian Palm	Comp Code	SIFT
1	99.42%	96.50%	98.33%	65.83%	92.83%	81.50%
2	99.58%	98.75%	99.25%	77.50%	95.42%	90.08%
3	100.00%	99.17%	99.92%	84.67%	98.42%	93.33%
4	100.00%	99.17%	99.92%	88.33%	98.50%	94.75%
5	100.00%	99.33%	99.92%	90.92%	98.92%	95.33%
6	100.00%	99.33%	99.92%	92.33%	99.50%	96.00%

TABLE XI
RANK-1 IDENTIFICATION RATE FROM FIRST 200 RIGHT PALMS OF THE POLYU DATABASE WITH 50 *UNKNOWN* SUBJECTS WITH VARYING NUMBERS OF GALLERY IMAGES PER CLASS

Number of Gallery Samples per Class	NMRT	Hessian Phase	Ordinal Code	Laplacian Palm	Comp Code	SIFT
1	99.92%	98.50%	99.92%	77.42%	92.67%	85.58%
2	99.92%	99.08%	99.92%	84.17%	96.00%	91.08%
3	100.00%	99.33%	99.92%	86.83%	97.67%	92.50%
4	100.00%	99.50%	99.92%	88.50%	98.83%	93.92%
5	100.00%	99.50%	99.92%	89.17%	98.92%	94.92%
6	100.00%	99.42%	99.92%	89.00%	99.00%	95.42%

that utilizes the neighborhood features to preserve the local structure. Obviously, the more (representative) samples for the specific class, the preserved local structures can be more stable which can more reliably identify the probe samples.

TABLE XII
RANK-1 IDENTIFICATION RATE FROM FIRST 200 LEFT AND FIRST 200 RIGHT PALMS OF THE POLYU DATABASE WITH 100 *UNKNOWN* SUBJECTS WITH VARYING NUMBERS OF GALLERY IMAGES

Number of Gallery Samples per Class	NMRT	Hessian Phase	Ordinal Code	Laplacian Palm	Comp Code	SIFT
1	99.63%	98.71%	99.33%	64.13%	92.96%	84.04%
2	99.75%	99.29%	99.50%	73.79%	95.42%	90.38%
3	100.00%	99.79%	99.92%	77.96%	97.71%	92.63%
4	100.00%	99.83%	99.96%	80.92%	98.29%	94.13%
5	100.00%	99.88%	99.96%	82.13%	98.67%	95.04%
6	100.00%	99.88%	99.92%	83.92%	99.00%	95.58%

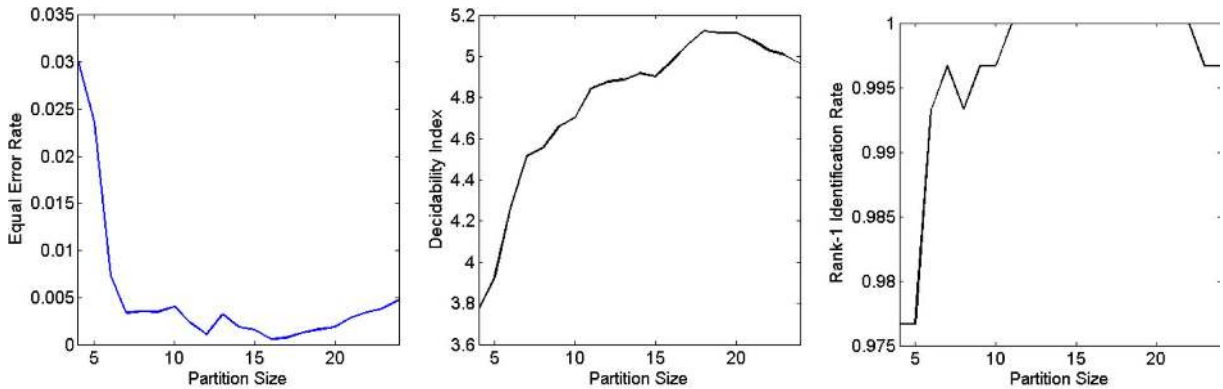

(a) (b) (c)

Fig. 9. Relationship between partition size of NMRT with (a) equal error rate, (b) decidability index, and (c) rank-1 recognition rate on the CASIA database.

C. Verification Experiments

We also performed rigorous experiments to evaluate the performance for the verification problem. First we investigate the comparative performance from the individual palms separately using various methods while varying the number of training samples. This resulted in 300 (100×3) genuine scores and 29 700 $(100 \times 99 \times 3)$ imposter scores on the CASIA database, and 1500 (250×6) and 373 500 $(250 \times 249 \times 6)$ genuine and imposter matching scores, respectively, from the PolyU database. We also ascertain the performance from two different hands of an individual (left and right) as belonging to different subjects, which result in 600 (200×3) genuine, 119 400 $(200 \times 199 \times 3)$ imposter scores, and 3000 (500×6) genuine, 1 497 000 $(500 \times 499 \times 6)$ imposter scores from the CASIA and PolyU databases, respectively.

The selection of appropriate partition size for NMRT is critical in achieving higher performance; if the selected size is too small, the partition may represent a lot of noise and thus not representative to the true dominant feature in the particular area. In other words, partitions which are too small in size tend to have higher genuine matches; however, it also leads to higher imposter/noisy matches which deteriorates the performance. On the contrary, partitions which are too large in size will suppress the representative local features and instead emphasize on the global ones, which is contrary to the motivation for our matching approach and is thus expected to deteriorate the performance. Fig. 9[4] illustrates the relationships between partition size and performance on the CASIA database, and the results are obtained by *using only the training* or enrollment data (i.e., the first session data). It can be observed from this figure that a smaller equal error rate is achieved at two places, one is 12 and the other is 16. However, the decidability index from size of 16 is much higher than that of 12, which implies better separation between the two score distributions (in case of Gaussian). Therefore, we fixed the partition size as 16 for the CASIA database; similar analysis was performed for the PolyU database and the partition size was fixed to 24.

The results (see Figs. 10 and 11, and Tables XIII and XIV) suggest performance improvement for all approaches with increasing the number of training samples, and the trend of this improvement was quite consistent with our observation from the identification experiments. The competitive code achieves very promising results in [9], but did not perform well on this set of experiments. A plausible reason for such performance is that reference [9] employed all the possible matches from the database for the performance estimation, which also match the data that is acquired in the same session, and this may lead to biased performance estimation. The matching of the same session data tends to achieve better matching as compared to that of a different session due to smaller variations (possibly contributed by the increased familiarity with the device in palm representation), and this will compensate the poor matches (if any) from the different data session, and thus lead to unreliable estimation.

Fig. 12 shows the genuine and imposter distribution using an NMRT approach on the CASIA and PolyU databases, respectively, and illustrates relatively clear separation between the genuine scores and imposter scores. The observed distribution of matching scores resembles or is similar to the Gaussian shape. However, the distribution of genuine matching scores illustrates larger variations (fluctuations) and this may be due to a relatively small number of genuine scores, i.e., 300 scores, from the CASIA database. The above observation also supports our approach to use the decidability index while selecting the parameter for NMRT.

[4]Defined as $d' = |\mu_A - \mu_I| / \sqrt{(\sigma_A^2 + \sigma_I^2)/2}$.

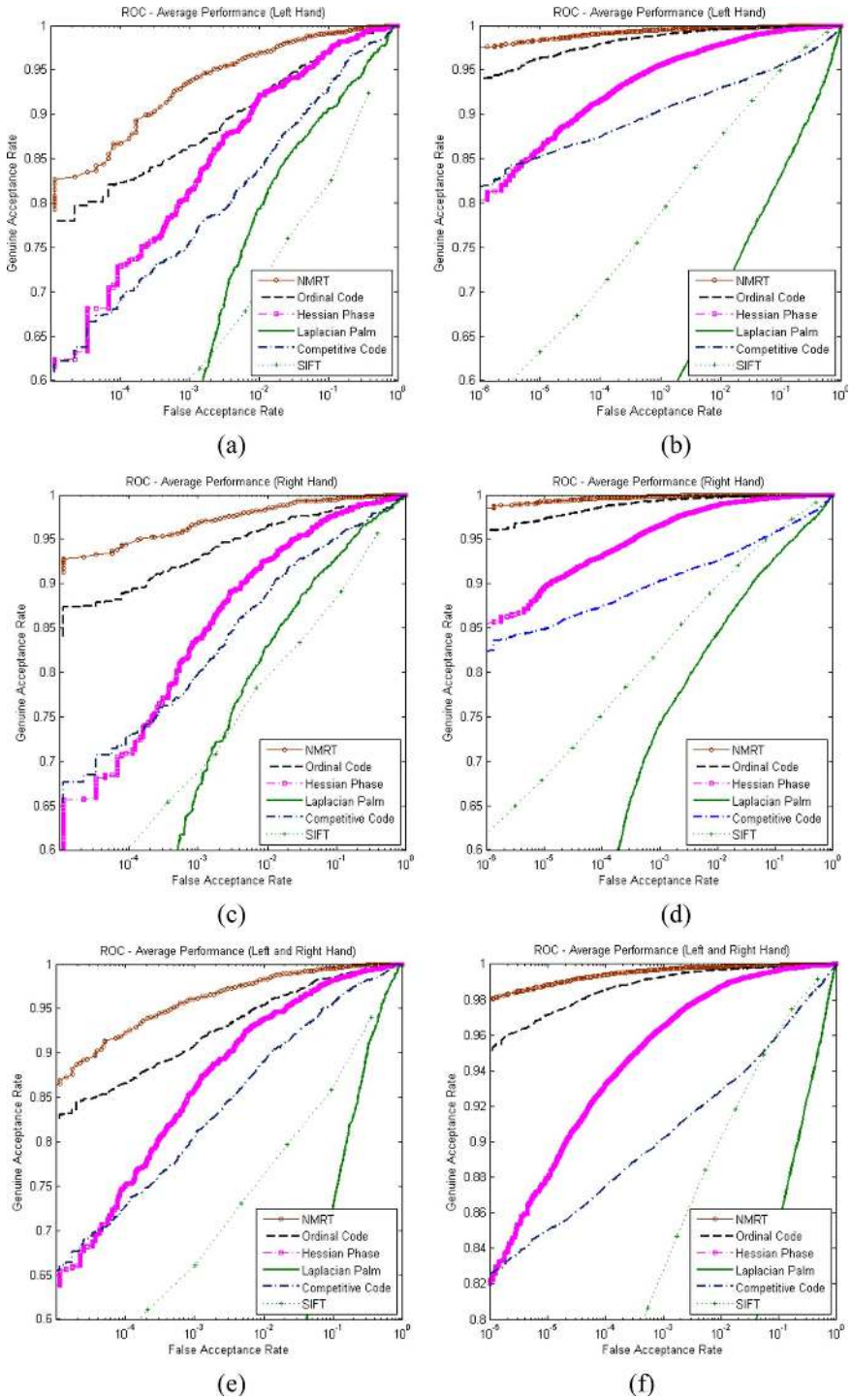

Fig. 10. Receiver operating characteristics from the CASIA and PolyU databases using *one training*: (a), (b) left palm; (c), (d) right palm; and (e), (f) left and right palm.

V. Discussion

The experimental results presented in Section IV consistently suggests that palm-vein identification using NMRT achieves significantly improved performance over the earlier proposed approaches on both contactless and constrained palm-vein images. In order to comparatively ascertain the performance from two databases using two different matching schemes [i.e., (6) and (8)], and corresponding ROC from the two databases are shown in Fig. 13. It can be observed from this figure that the neighborhood matching scheme performs consistently better than the counterpart. This superior performance can be attributed to the robust and relatively more stable extraction of palm-vein features by searching for the dominant direction in the local area and quantizing the orientation. In addition, the palm-vein images can be quite unclear even after the enhancement, primarily due to variations during the imaging or environment. In such cases, the features that extracted by NMRT reflect the local texture patterns rather than the dominant vein directions, and this ensures the robust performance from

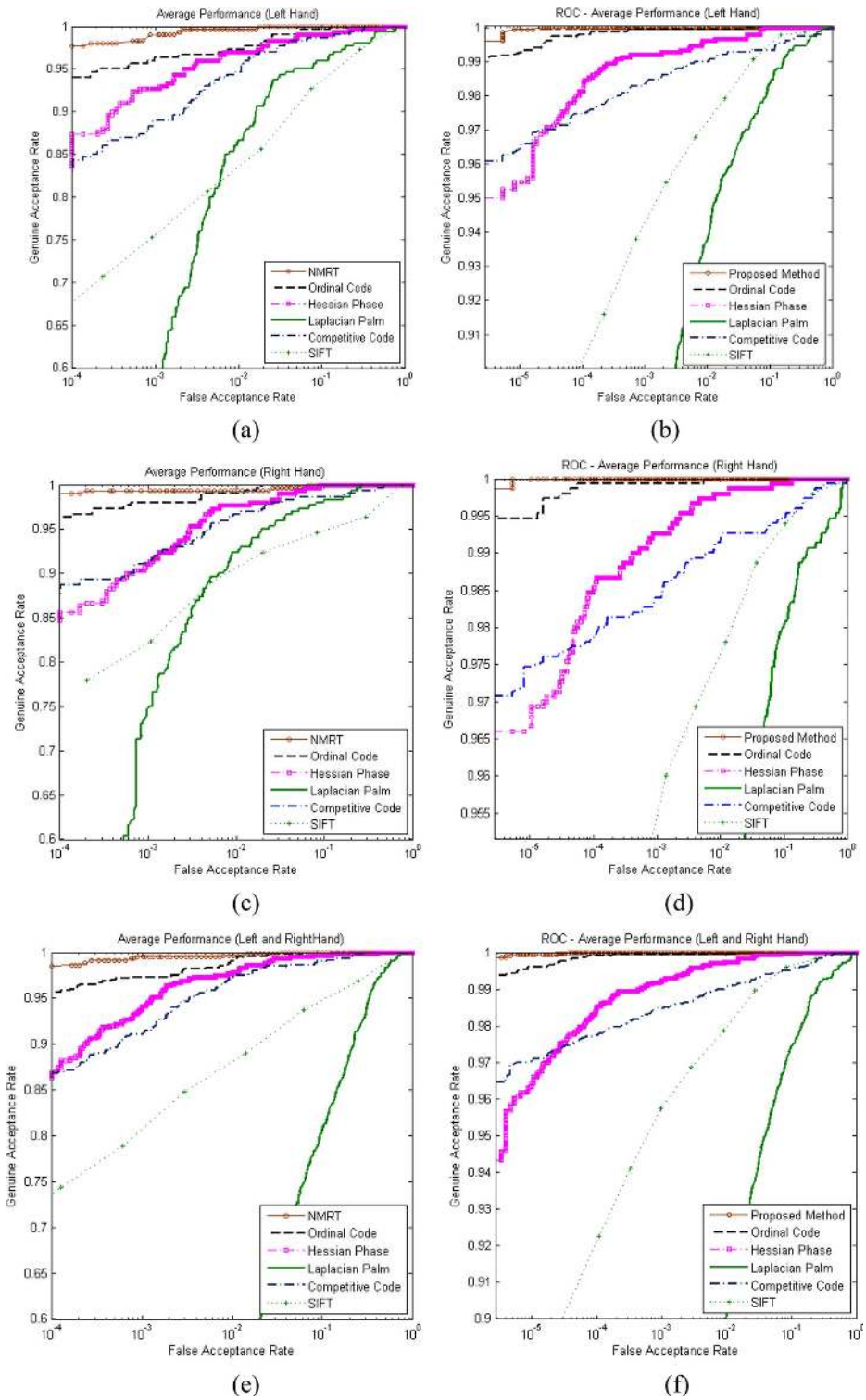

Fig. 11. Receiver operating characteristics from the CASIA and PolyU databases using *all training samples* during first session: (a), (b) left palm; (c), (d) right palm; and (e), (f) left and right palm.

this approach. Furthermore, the neighborhood matching scheme exploits the local information which represents more distinct characteristics and more robustness to intraclass changes. This scheme still performs relatively better even under the minimum training cases, which is also contributed by the neighborhood matching, since it partitions the templates into small subregions and thus has effectively higher training samples to some extent as compared to the matching that uses the template as a whole.

In addition, from the computational efficiency point of view, NMRT uses almost the same computation as its counterpart [i.e., (6)] but achieves much better results. Let N denote the size of the ROI, and let w and h represent the amount of horizontal and vertical shifting; for (6), it needs $N^2 \times w \times h$ number of operations to calculate the matching score. While for NMRT, it needs $\lceil N/b \rceil^2 \times b^2 \times w \times h$ number of operations, where b is the size of the block and $\lceil\ \rceil$ is the ceiling operator. If we choose

TABLE XIII
EQUAL ERROR RATE FROM LEFT AND RIGHT PALMS IN THE CASIA DATABASE USING DIFFERENT APPROACHES WITH VARYING NUMBERS OF TRAINING SAMPLES

Number of Training Samples	NMRT	Hessian Phase	Ordinal Code	Laplacian Palm	Comp Code	SIFT
1	1.37%	3.66%	3.11%	17.89%	6.01%	13.55%
2	0.68%	2.11%	1.67%	15.93%	3.11%	7.99%
3	0.51%	1.44%	1.00%	14.79%	2.00%	6.19%

TABLE XIV
EQUAL ERROR RATE FROM LEFT AND RIGHT PALMS IN THE POLYU DATABASE USING DIFFERENT APPROACHES WITH VARYING NUMBERS OF TRAINING SAMPLES

Number of Training Samples	NMRT	Hessian Phase	Ordinal Code	Laplacian Palm	Comp Code	SIFT
1	0.21%	1.17%	0.43%	12.93%	4.98%	5.58%
2	0.06%	0.73%	0.18%	8.43%	2.74%	3.32%
3	0.03%	0.57%	0.13%	6.73%	1.80%	2.24%
4	0.02%	0.48%	0.11%	5.70%	1.30%	1.94%
5	0.01%	0.41%	0.08%	5.15%	1.11%	1.68%
6	0.004%	0.43%	0.07%	4.56%	0.95%	1.58%

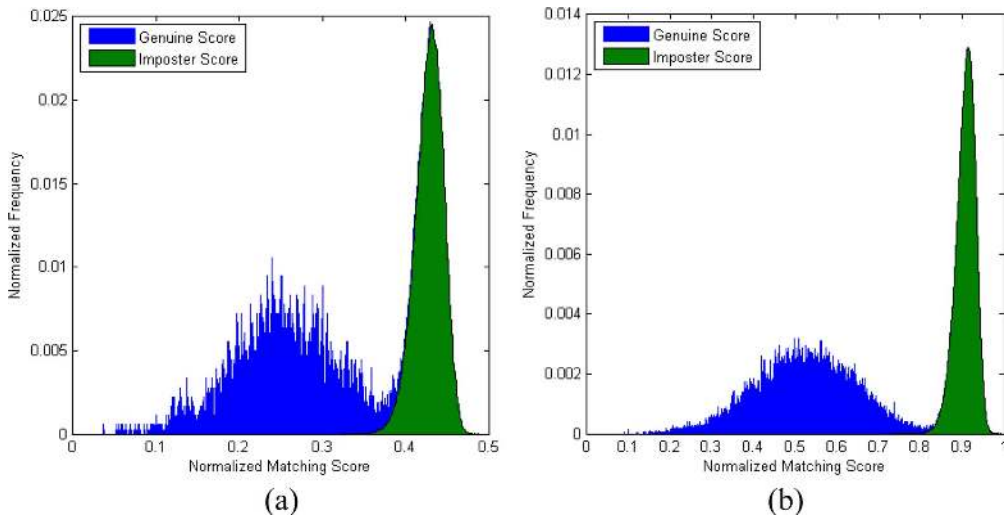

Fig. 12. Genuine and imposter distributions from left- and right-hand palm-vein images using NMRT from (a) the CASIA and (b) PolyU databases.

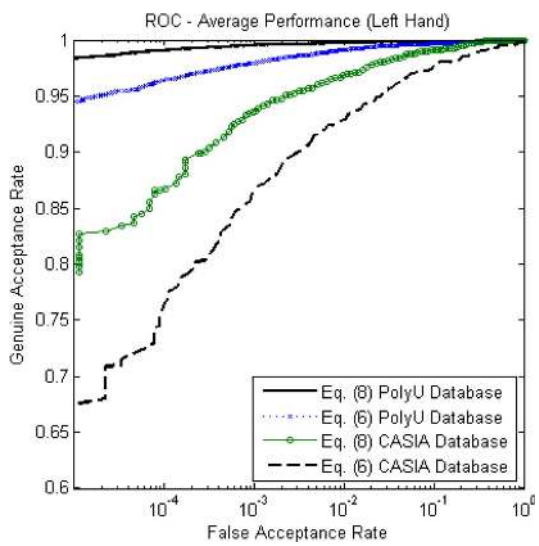

Fig. 13. Receiver operating characteristics from two databases for left-hand palm-vein images with different matching approaches.

the value of b such that it can be divided by N, then the two approaches use exactly the same number of operations while matching.

We also investigated a new approach to characterize the palm-vein images using local curvature information, i.e., the Hessian matrix. This approach enhances the vessel (palm-veins) patterns of different widths by employing multiscale measures. Additionally, it also saves computation in finding the direction of the local vein patterns by analyzing the eigenvalues of the Hessian matrix instead of evaluating multiple filter responses in different orientations. The binarized templates generated from this approach *require the least amount of storage* (only one bit for each corresponding position; see Table XV for comparison with other methods), *as compared to other previously proposed methods in the palm-vein literature*, while achieving relatively higher performance (consistently outperform other methods except NMRT and Ordinal Code). Therefore, this approach can be a computationally efficient alternative for the compact palm-vein template representation and matching. The Hessian-phase-based approach does not outperform NMRT and Ordinal Code, and this may be explained by several factors as discussed in the previous paragraph. While the veins in the image are not very clear, it can be quite difficult for the Hessian phase representation to extract local features, since it is not suitable for texture representation (unlike the NMRT and Ordinal approaches).

The observed performance from the Laplacian palm approach was not high on the CASIA database, and this may be due to the fact that it does not focus on extracting and matching the local textured information, and lack strong mechanism

TABLE XV
ILLUSTRATION OF TEMPLATE SIZE FROM VARIOUS APPROACHES (IN BYTES)

Method / Database	NMRT	Hessian Phase	Ordinal Code	Laplacian Palm**	Comp Code	SIFT††
CASIA	384	2,048	6,144	17,584	6,144	~68,608
PolyU	486	2,592	7,776	22,384	7,776	~77,184

** The template size for a single image is obtained by dividing the total size needed for storing the coefficients by the total number of training images.
†† The number of SIFT descriptors vary from image to image, hence the size is estimated using the average number of descriptors.

TABLE XVI
SUMMARY OF RELATED APPROACHES FOR THE PALM-VEIN VERIFICATION

Reference	Methodology	Pegs	Database Size (Number of uses)	Performance (EER %)
[10]	Using Laplacianpalm representation on fused palmvein and palmprint images, employed KNN classifier for matching.	No	120	~0.40[1]
[11]	Present the fused palm images by OLOF features, and hamming distance is computed for similarity measure.	No[2]	165	0.50
[9]	Extract features from multi-spectral palmprint images using Gabor filters, and employed score level fusion to obtain matching score.	Yes	250 (PolyU database)	0.012
[12]	Using ant colony optimization to select the Gabor features extracted from the fused palm images, and use SVM classifier for matching.	No[2]	100 (CASIA database)	3.12
[13]	Palmvein features are extracted by morphological gradient operation, and palmprint features are analyzed by Haar wavelet. The final matching score is obtained by using sum rule.	Yes	50	~4.00[1]
[14]	Extract palmvein features from multiscale matched filters, and hamming distance is employed as matching score.	Yes	144	4.00[1]
[15]	Multiscale matched filter is employed for palmvein feature extraction, and the matching score is generated using ICP algorithm.	Yes	250 (PolyU database)	0.557
[16]	Feature vectors composed of junction points extracted from the fused palmprint and palmvein images, the matching score is generated by using logical 'AND' operators between two templates.	No	106	~0.50[1]
[17]	SIFT descriptors are employed to represent the features from palmvein images, and Euclidean distance is used for similarity measure.	No	24	0.00
This paper	Feature extraction and matching using NMRT and Hessian phase from palmvein images.	No[2] Yes	100 (CASIA database) 250 (PolyU database)	0.51(NMRT) 1.44(Hessian) 0.004(NMRT) 0.43(Hessian)

[1] EER estimated from the ROC plots provided in the paper.
[2] System acquires the palm images in a contact free manner.

to accommodate potentially large variations which are more likely to exist in the contactless database. We have also evaluated this approach on the same-session data from the PolyU database and achieved zero percent EER (0% EER for both hands, which is similar to the performance reported in [10]), which further confirms that this method is not very good at accommodating large intraclass variations.[5] It also does not perform well in the case of a smaller number of training samples, which is again the case in the CASIA database (maximum three training samples are available), and this may be attributed to the difficulties in building a reliable neighborhood pattern structure in the Laplacianpalm process. Table XVI summarizes the palm-vein approaches in the literature and suggests that the superior performance is achieved from the approaches detailed in this paper. The performance improvement trends with the increase in number of training samples is quite consistent in both verification and identification experiment, and on both of the two employed databases. In most cases, the largest performance gain was obtained when the number of training samples was increased from one to two, which suggests that the large amount of complementary information contributed by the additional sample. On the other hand, the additional training

[5]The NMRT approach also achieves 0% EER when evaluated on one session-data.

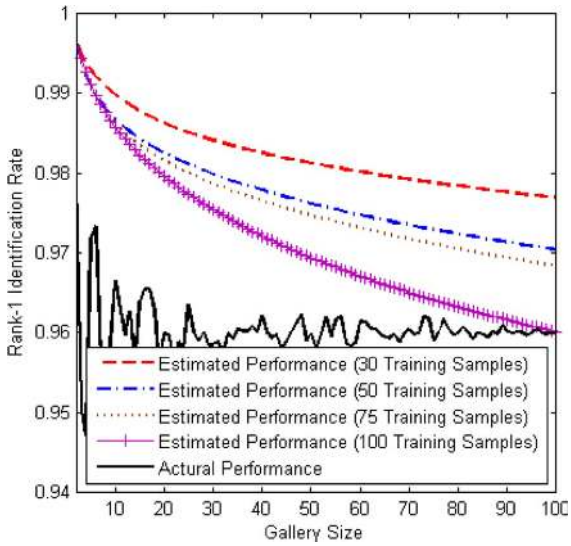

Fig. 14. Estimated left-hand palm-vein identification performance as a function of gallery size, from the CASIA database.

samples (beyond two) do not offer as much improvement as the previous one, which suggests that the additional information may be more redundant rather than complimentary, with the further increase in training samples in these two databases.

A. Comment on Identification Performance Estimation

We also performed experiments to estimate the rank-1 identification rate for the larger population using simulation from the best of the proposed approach. This simulation for the estimation of rank-1 identification rate employed the same approach as in [25] which estimates the rank-1 identification performance $r(\zeta)$ from the following equation:

$$r(\zeta) = \int_{-\infty}^{+\infty} (1 - far(\varepsilon))^{\zeta} g(\varepsilon) d\varepsilon \tag{20}$$

where $g(\varepsilon)$ is the probability density function from genuine matching scores, and ς represents the gallery size. The estimated rank-1 recognition performance with one gallery sample per class using the above equation to a gallery size of 200 and 500 from left palm of the CASIA and PolyU databases was 93.92% and 99.38%, respectively. However, we observed that this estimation may not be reliable, as can be observed from Fig. 14 unless we use all the samples in the database to ascertain the final estimation and such estimated result will unlikely be close to the true value, and such estimation provides the best possible or most optimistic results. The reason for this may lie in the fact that this model basically employs the idea of maximum likelihood estimation and does not generate any prior true match or nonmatch distribution. This problem becomes more severe while simulating the performance of a large population from the real distribution that offers very good performance. From (20), we can observe that while the estimation gallery size is large, the first term in the equation tends to vanish, and thus the estimated result will be nearly equal to the area of the match distribution minus the intersection between match and nonmatch distribution (equal to equal error rate). In an extreme case, if we achieve a perfect separation between the true match and nonmatch score distributions (from the smaller size real samples), this estimation will result in 100% rank-1 identification rate irrespective of the size of the gallery, which can be perceived as a major shortcoming of using a pure maximum likelihood approach and the corresponding result is obviously not reasonable. In summary, this simulation scheme uses a pure maximum likelihood approach that does not assume any prior distribution on the match and nonmatch distributions, which makes the estimation less reliable, especially in the case of very low EER performance. Therefore, the reliability of this prediction can be improved by incorporating a prior distribution of both match and nonmatch scores to compute the maximum posterior estimation or by employing a fully Bayesian approach.

VI. Conclusion

This paper investigated a novel approach for human identification using palm-vein images. We propose a novel feature extraction and matching approach that can effectively accommodate the potential image deformations, translational, and rotational variations by matching to the neighborhood of the corresponding regions and generating more reliable matching scores. This approach performs very well even with the minimum number of enrollment images (one sample for training). The performance was rigorously evaluated and compared to the existing method on two different databases with a different imaging setup, and evaluated with all possible numbers of training samples. Our proposed method shows its robustness and superiority in both cases. The Hessian phase approach extracts palm-vein features by analyzing the eigenvalues of the local image instead of filtering the image by predefined filters in different orientations, also achieves reasonably superior performance, and at the same time provides a smaller template size as compared to other methods. Therefore, it offers a computationally simpler and compact storage (template size) alternative for the palm-vein identification applications. We achieved a rank-1 identification rate of 99%, 99.33%, and 100% from the left, right-palm-vein images of the CASIA and PolyU databases, respectively, and correspondingly achieved EER of 0.32%, 0.66%, 0.002%, and 0.001%. The performance gain achieved from the additional training samples is quite significant while the sample size is still small, but the redundant information accumulates rapidly as the training sample size increases. How to effectively make use of such complementary information available from the additional training samples, while ensuring that such redundancy is in a limited amount, is critical in achieving further performance improvement and requires further research efforts. The finger images are also acquired from the contactless palm-vein imaging (CASIA database) and can also be employed for further performance improvement. Such a combination of palm-vein and surface finger-vein is worth exploring for a large contactless database and is suggested for the further/future work.

Acknowledgment

The authors thankfully acknowledge the Chinese Academy of Sciences for providing the CASIA-MS-PalmprintV1 database used in this work.

REFERENCES

[1] A. K. Jain and J. Feng, "Latent palmprint matching," *IEEE Trans. Pattern Anal. Mach. Intell.*, vol. 31, no. 6, pp. 1032–1047, Jun. 2009.

[2] R. Singh, M. Vatsa, H. S. Bhatt, S. Bharadwaj, A. Noore, and S. S. Nooreyezdan, "Plastic surgery: A new dimension to face recognition," *IEEE Trans. Inf. Forensics Security*, vol. 5, no. 3, pp. 411–418, Sep. 2010.

[3] T. Matsumoto, H. Matsumoto, K. Yamada, and S. Hoshino, "Impact of artificial "gummy" fingers on fingerprint systems," *Proc. SPIE*, pp. 275–289, 2002.

[4] S. Z. Li, *Encyclopedia of Biometrics*. New York: Springer, 2009.

[5] Z. Wei, X. Qiu, Z. Sun, and T. Tan, "Counterfeit iris detection based on texture analysis," in *Proc. Int. Conf. Pattern Recognition*, Tampa, 2008, pp. 1–4.

[6] G. Pan, L. Sun, Z. Wu, and S. Lao, "Eyeblink-based anti-spoofing in face recognition from a generic webcamera," in *Proc. Int. Conf. Computer Vision*, Rio de Janeiro, 2007, pp. 1–8.

[7] T. B. Habif, *Clinical Dermatology*. St. Louis: Mosby-Year Book, Inc., 1996.

[8] V. P. Zharov, S. Ferguson, J. F. Eidt, P. C. Howard, L. M. Fink, and M. Waner, "Infrared imaging of subcutaneous veins," *Lasers Surgery Medicine*, vol. 34, no. 1, pp. 56–61, Jan. 2004.

[9] D. Zhang, Z. Guo, G. Lu, L. Zhang, and W. Zuo, "An online system of multispectral palmprint verification," *IEEE Trans. Instrum. Meas.*, vol. 59, no. 2, pp. 480–490, Feb. 2010.

[10] J.-G. Wang, W.-Y. Yau, A. Suwandy, and E. Sung, "Person recognition by fusing palmprint and palm vei images based on "Laplacianpalm" representation," *Pattern Recognit.*, vol. 41, pp. 1514–1527, Oct. 2007.

[11] Y. Hao, Z. Sun, T. Tan, and C. Ren, "Multispectral palm image fusion for accurate contact-free palmprint recognition," in *Proc. ICIP 2008*, 2008, pp. 281–284.

[12] SIFT Keypoint detector: Demo software [Online]. Available: http://www.cs.ubc.ca/~lowe/keypoints

[13] K.-A. Toh, H.-L. Eng, Y.-S. Choo, Y.-L. Cha, W.-Y. Yau, and K.-S. Low, "Identity verification through palm vein and crease texture," in *Lecture Notes in Computer Science*. Berlin/Heidelberg: Springer, 2005, pp. 546–553.

[14] Y.-B. Zhang, Q. Li, J. You, and P. Bhattacharya, "Palm vein extraction and matching for personal authentication," in *Lecture Notes in Computer Science*. Berlin/Heidelberg: Springer, 2007, pp. 154–164.

[15] H. Chen, G. Lu, and R. Wang, "A new palm vein matching method based on ICP algorithm," in *Proc. Int. Conf. Interaction Sciences*, Seoul, 2009, pp. 1207–1211.

[16] J.-G. Wang, W.-Y. Yao, and A. Suwandy, "Feature-level fusion of palmprint and palm vein for person identification based on a "junction point" representation," in *Proc. ICIP*, 2008, pp. 281–284.

[17] P.-O. Ladoux, C. Rosenberger, and B. Dorizzi, "Palm vein verification system based on SIFT matching," *Lecture Notes in Computer Science*, vol. 5558/2009, pp. 1290–1298, 2009.

[18] Y. Zhou and A. Kumar, "Contactless palmvein identification using multiple representation," in *Proc. BTAS'10*, Washington, DC, Sep. 2010.

[19] J. Radon, "Über die bestimmung von funktionen durch ihre integralwerte längs gewisser mannigfaltigkeiten," *Berichte über die Verhandlungen der Sächsische Akademie der Wissenschaften*, no. 69, pp. 262–277, 1917.

[20] W. Jia, D.-S. Huang, and D. Zhang, "Palmprint verification based on robust line orientation code," *Pattern Recognit.*, vol. 41, no. 5, pp. 1504–1513, May 2008.

[21] A. Kumar and Y. Zhou, "Human identification using knucklecodes," in *Proc. BTAS 2009*, Washington, DC, 2009, pp. 47–152.

[22] A. F. Frangi, W. J. Niessen, K. L. Vincken, and M. A. Viergever, "Multiscale vessel enhancement filtering," in *MICCAI*. Berlin, Germany: Springer Verlag, 1998, pp. 130–137.

[23] M.-L. Feng and Y.-P. Tan, "Contrast adaptive binarization of low quality document images," *IEICE Electron. Express*, vol. 1, no. 16, pp. 501–506, Nov. 2004.

[24] CASIA MS Palmprint V1 Database [Online]. Available: http://www.cbsr.ia.ac.cn/MS_Palmprint

[25] Face Recognition Vender Test 2002 Evaluation Report [Online]. Available: http://www.frvt.org/DLs/FRVT_2002_Evaluation_Report.pdf

[26] A. Kumar and K. V. Prathyusha, "Personal authentication using hand vein triangulation," *IEEE Trans. Image Process.*, vol. 38, no. 9, pp. 2127–2136, Sep. 2009.

[27] M. Hiraoka, M. Firbank, M. Essenpries, M. Cope, S. Arridge, P. van der Zee, and D. Deply, "A Monte Carlo investigation of optical pathlength in inhomogenous tissue and its application to near-infrared spectroscopy," *Phys. Medicine Biol.*, vol. 38, pp. 1859–1876, 1993.

Yingbo Zhou received the B.E. degree in computer science from the Civil Aviation University of China, in 2006, and the M.S. degree in computer science (with distinction) from the Hong Kong Polytechnic University, in 2010. He is currently working toward the Ph.D. degree in computer science at the State University of New York at Buffalo.

His research interests include pattern recognition, computer vision, and machine learning.

Ajay Kumar (S'00–M'01–SM'07) received the Ph.D. degree from the University of Hong Kong, in May 2001.

From October 2001 to December 2002, he was a Postdoctoral Researcher in the Department of Computer Science, Hong Kong University of Science and Technology, Hong Kong. From 2003 to 2005, he was a Postdoctoral Fellow at the Hong Kong Polytechnic University, where he was in the Department of Computing from April 2004 to January 2005. From 2005 to 2007, he was an Assistant Professor, Department of Electrical Engineering, Indian Institute of Technology Delhi, India. He is currently an Assistant Professor with the Department of Computing, The Hong Kong Polytechnic University, Kowloon, Hong Kong. He is currently on the editorial board of IEEE TRANSACTIONS ON INFORMATION FORENSICS AND SECURITY, and serves on the IEEE Biometrics Council as Vice President (Publications). He has been an area-editor, Hand Biometrics, for the Encyclopedia of Biometrics (Springer, 2009) and served on the program committees of several international conferences and workshops in the field of his research interest. He was the program chair of The Third International Conference on Ethics and Policy of Biometrics and International Data Sharing in 2010 and was the program cochair of the International Joint Conference on Biometrics, IJCB 2011, held in Washington DC, in 2011. His current research interests are on biometrics with the emphasis on hand biometrics, vascular biometrics, iris and multimodal biometrics.

Dr. Kumar holds two U.S. Patents and has published extensively on biometrics and computer vision-based industrial inspection.